3D-Focused ion beam tomography and quantitative porosity evaluation of ZrO_2-SiO_2 composite coating; amorphous SiO_2 as a porosity tailoring agent

M. Farhadian[1,2], K. Raeissi[1], M. A Golozar[1], S. Labbaf[1], T. Hajilou[2], A. Barnoush[2,] *

[1] Department of Materials Engineering, Isfahan University of Technology 84156-83111, Isfahan, Iran

[2] Department of Mechanical and Industrial Engineering, NTNU, Richard Birkelands Vei 2b, 7491 Trondheim, Norway

Abstract

The current study is focused on refining effect of amorphous SiO_2 on porosity and interlayer formation of sintered ZrO_2-SiO_2 composite coatings produced on anodic oxidized 316L substrate. The SiO_2 improved particle interaction with the substrate surface and increased thickness of the interlayer formed at the coating/substrate interface. For porosity evaluation, the coatings were sliced and imaged layer by layer using focused ion beam-scanning electron microscopy and 3D visualizations reconstructed by stacking the acquired 2D images. Volume fraction, dimension, distribution and connectivity of pores as a function of coating composition were analyzed. The results showed that SiO_2 also densifies the coating and decreases volume fraction of connected pores. Corrosion performance of ZrO_2-SiO_2 coatings was improved with increasing SiO_2 content due to the higher barrier effect resulted by increasing the interlayer thickness as well as the lower permeability supported by lower percent of connected pores.

Keywords: Porosity; Tomography; Zirconia; Silica; Multi-phase oxide; Corrosion

* Corresponding Author: afrooz.barnoush@ntnu.no
Mousa Farhadian: (mousa.farhadian@ma.iut.ac.ir)
Keyvan Raeissi: (k_raeissi@iut.ac.ir)
Mohammad Ali Golozar: (golozar@iut.ac.ir)
Sheyda Labbaf: (s.labbaf@iut.ac.ir)
Tarlan Hajilou: (tarlan.hajilou@ntnu.no)
Afrooz Barnoush (afrooz.barnoush@ntnu.no)

1. Introduction

Tailored porous structures reveal unique features that are advantageous compared to their conventional dense counterpart [1]. Nowadays, bio-ceramic coatings are widely applied on metallic implants to enhance various surface characteristics such as biocompatibility, osseointegration, and corrosion resistance [2-6]. In this regard, porosity is known as a great contributing factor in developing multifunctional coatings for biomedical applications [7, 8]. Coatings with sufficient volume fraction of interconnected pores can promote tissue ingrowth and provide biological anchorage, leading to formation of a strong biological tissue-implant interface [9]. Also, surface porosities have shown to reduce the effect of stress shielding, which often occurs due to the elastic modulus difference between bone and ceramic coatings resulting in increased stress distribution to bone and hence minimizing overload episodes [8, 10, 11]. Meanwhile, porosity has a negative effect on cohesion strength of the coatings [12, 13], and it can deteriorate the barrier performance of the coating against diffusion of corrosive elements through available interconnected channels toward the substrate [14, 15]. Consequently, the size, shape, distribution and interconnectivity of the porous structure have to be precisely controlled to maximize the functionality of the coatings.

Different processing techniques have been used to fabricate porous ceramic coatings [16]. Among them, electrophoretic deposition (EPD) is a promising method due to its simplicity, cost-effective, and deposition capability of various ceramic and composite materials [17]. The EPD is based on migration of charged particles in colloidal suspension under an applied electrical field and deposition on the oppositely charged substrate [18]. The obtained deposits should then be sintered to densify and increase the adhesion and cohesion strength [19]. In this method, pore structure can be mainly controlled by suspension and process parameters such as type and amount of electrolyte and additives (e.g., surfactants and dispersants), particle concentration, applied voltage, as well as type and distance of electrodes [20]. For

example, conically shaped porous structure of Al_2O_3 with dimensions from 500 nm up to 200 µm has been developed from aqueous suspensions due to hydrogen evolution during the cathodic EPD process [21]. EPD is also applied to fabricate highly ordered microporous HAp coating on titanium implant from a suspension containing polystyrene spheres (3 µm in diameter) as a sacrificial template [22]. Recently, vertically aligned reduced graphite oxide nanosheets on substrate developed by combination of EPD and ice template method show pore sizes ranging from 10 to 100 µm [23]. Previous studies have, hence, mainly focused on developing porous coatings by only changing the electrophoretic parameters; however, there are limited studies on the impact of particle chemical composition on pore refining. Although multiphase oxide coatings such as ZrO_2-Y_2O_3-CeO_2 [24], Al_2O_3-ZrO_2 [25], SiO_2-TiO_2 [26] and HA-ZrO_2 [27] have been previously produced, the effect of each component on porous structure has not been studied. Often, various methods such as mercury intrusion porosimetry (MIP) [28], X-ray computed micro-tomography (micro-CT) [29] and focused ion beam (FIB) tomography [30] are applied for porosity networks evaluations. MIP can provide some evidence about pore structure (i.e. pore diameter, pore size distribution and densities), but it is still inefficient to characterize isolated pores due to their inaccessibility. MIP theoretically measures pore size ranging from 100 µm down to a few nanometers [9], and also the entrance toward a pore without detecting its actual inner size or shape resulting in an overestimation of the frequency on small pores [31]. Micro-CT technique is a non-destructive 3D visualization and is suitable for measuring the pores greater than 500 nm in diameter; however, small pores are often not detected, which results in underestimation of total porosity owing to the limitation of image resolution [32]. On the other hand, FIB-tomography can be categorized as a suitable technique for 3D imaging of porous structure in the range higher than 10 nm in equivalent diameter, which can help to overcome the limitations of these two methods [33, 34]. In this method, rich microstructural data from the internal pores of coating can be

achieved by quantitative analysis of reconstructed 3D images (i.e. volume fraction of connected and isolated pores, shape, pore size, pore size distribution) [35]. The porosity evaluation using FIB tomography is relatively costly compared to Micro-CT and MIP techniques [36, 37]. However, its high potential in analyzing the isolated pores and detecting finer pores can provide detailed information to reconstruct more actual 3D pore network. This facilitates the study of sintering behavior of various ceramic materials especially multi-phase ceramic coatings [38].

ZrO_2-SiO_2 multi-phase coatings have been prepared by different coating techniques; however, tailoring effect of amorphous SiO_2 on its porosity structure is still inconclusive. In this work, ZrO_2-SiO_2 composite particles with different SiO_2 content (e.g. 0, 10, 20, and 30 mol. %) are prepared by sol-gel method, and then, deposited on surface-treated 316L stainless steel substrate using EPD method. The substrate is modified by anodic oxidation treatment to create a porous surface structure before coating process. Effect of silica content on sintering behavior and interlayer formation at the interface of coating/substrate is studied. The 3D visualization of the coatings reconstructed by FIB tomography technique, and precise information about porosity structure of ZrO_2-SiO_2 coatings versus silica content are thoroughly investigated.

2. Materials and methods

2.1 Materials

Zirconium propoxide (70 wt. % in propanol), tetraethyl orthosilicate (TEOS), 2-methoxyethanol, ethanol, polyethyleneimine (PEI, Mw=10,000), iodine and ammonia solution were prepared from Sigma Aldrich. Sulfuric acid (98 wt. %), phosphoric acid (98 wt. %) and glycerol were prepared from Merck.

2.2 Preparation of ZrO_2/SiO_2 composite particles

ZrO_2/SiO_2 nanocomposite particles were synthesized using alkaline based sol-gel method. In brief, a certain amount of zirconium propoxide and TEOS were separately dissolved in 40 ml of 2-methoxyethanol, and were then mixed. An aqueous ammonia solution with pH of 11 was diluted by 2-methoxyethanol, added into the resulted solution and stirred until a clear gel was formed. The organic byproducts of the reaction were extracted from the gel by mixing with $EtOH/H_2O$ solution (90/10 vol. %) at 60 °C for 3 times and the gel was dried at 100 °C. The produced ZrO_2 and ZrO_2-SiO_2 particles were heat-treated for 4 h at 1000 and 1100 °C, respectively. The produced ZrO_2/SiO_2 composites with SiO_2 contents of 10, 20, and 30 mol. % are labeled as Z10S, Z20S, and Z30S, respectively.

2.3 Surface treatment of substrate

Chemical composition of 316L stainless steel (wt. %) used as the substrate was as follows: Cr: 16.6, Ni: 13.1, Mn: 1.73, Mo: 1.97, Si: 0.2, C: 0.024 and Fe: reminder. The substrate was mechanically polished using SiC papers up to 1200 grit and anodically oxidized in a bath containing 60 wt. % H_3PO_4 (from Merck), 20 wt. % H_2SO_4 (from Merck), 10 wt. % glycerol (from Merck) and 10 wt. % deionized water. For cleaning the substrate surfaces, they were washed using water and degreased 10 min in ethanol and acetone, respectively. The substrate was then anodically oxidized using 12 V for different times (3, 6, and 12 min) to obtain a surface showing suitable porosity and roughness. According to Infinite Focused Microscopy (IFM) images displayed in Fig. S1, the substrate oxidized for 6 min shows a more homogeneously distributed porosity. This sample is considered as the optimum substrate for further coatings.

2.4 Electrophoretic deposition of ZrO_2/SiO_2 composite particles

Large and dense agglomerated particles formed during heat treatment were ball milled in a placatory machine using zirconia jar and balls with a weight ratio of 20:1 (balls to powder) up to 2 h. Then, they were wet-ball milled for 24 h in ethanol containing 3 wt. % polyethylenemine (PEI) (Sigma Aldrich, MW=10000) as a surfactant using a polymeric cup and zirconia balls. A suspension with particle dosage of 5 g l^{-1} was prepared in EtOH as solvent. The pH of the suspensions was adjusted at 4 by adding iodine to provide the highest positive charge on the nanoparticles surface. Before electrophoretic deposition, the modified particles were well dispersed in the suspension using ultrasonic bath for 1 h. Two disk-shaped 316L substrates with 14 mm diameter and 3 mm thickness were used as working and counter electrodes with 2 cm distance in all tests. Electrophoretic deposition was conducted at a constant voltage of 15 V using DC power supply and coatings with ~ 20 µm thickness were produced (Fig. S2). The wet deposited samples were dried at 100 °C for 2 h, and finally, sintered at 1100 °C for 2 h in vacuum (10^{-5} torr) under heating and cooling rates of 2 °C/min.

2.5 Characterization techniques

Zeta potential and particle size distribution of suspensions were measured using Zeta sizer (Beckman counter Delsanano, N5 Submicron). X-ray diffraction (XRD, Philips X'pert, Cu kα) analysis was carried out using Philips PW1800 diffractometer operating with Cu Kα radiation at 40 kV and 30 mA at scanning rate of 3 °/min with a step size of 0.02 ° in 2θ range from 20 to 80 °. Topography and surface roughness of coatings were measured by Infinite Focused Microscopy (IFM, Alicona). Surface morphology, cross sectional view and elemental analysis of the coatings were studied using scanning electron microscope (SEM, FEI Helios) equipped by an energy dispersive spectroscopy (EDS) detector.

In order to study the pore structure of obtained coatings, 3D FIB tomography was performed by slice and view method [38, 39] using a dual beam FIB system (FEI Helios). The volume

region which is to be reconstructed is called “region of interest (ROI)”. To prevent surface damage due to ion beam incidence, a thick Pt layer (~ 2 µm) was applied on top of the ROI as a protective layer (Fig. 1a). Around the ROI was milled using ion beam source to prepare a trench with sufficient space and depth as indicated in Fig. 1b. The volume of ROI was automatically sliced layer by layer and the stacks of 2D slices (Fig. 1c) were aligned and then concatenate to reconstruct the final 3D modeling (Fig. 1d). These post-acquisition alignment and 3D reconstruction process were conducted by ImageJ-win64 and Dragonfly (Dragonfly 3.6.1, 2018) [40] software packages, respectively.

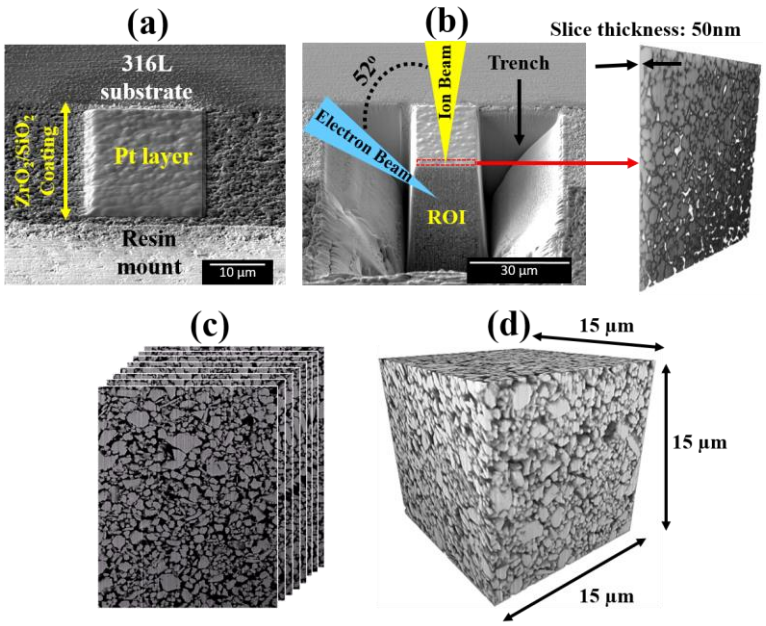

Fig. 1. SEM images of: (a) protective Pt layer on the ROI, (b) ROI area prepared by milling process along with one slice of this region, (c) stacks of 2D slices milled from ROI and (d) 3D reconstructed image from ROI.

2.6 Corrosion studies

The electrochemical corrosion behavior of bare and coated samples was studied through potentiodynamic polarization test and electrochemical impedance spectroscopy (EIS) using a potentiostat/galvanostat (Gamry instruments, Interface 1000). All tests were done at the similar conditions in simulated body fluid (SBF) at 37 ˚C after immersion for 24 h to establish open circuit potential (OCP) prior to running each test. All measurements were

carried out in a three typical electrode cell, in which, saturated calomel electrode (SCE) was served as reference electrode, platinum plate as counter electrode and uncoated/coated samples as working electrode. Polarization curves were obtained over potential range from -500 to 1500 mV versus OCP using scan rate of 1 mV s^{-1}. The impedance spectra were obtained using the same setup in the frequency range of 100 kHz to 10 mHz at OCP condition with an AC amplitude of 10 mV. The impedance data were fitted using Zview software and equivalent circuit (EC) model. Each measurement was repeated three times for evaluating the reproducibility of data.

3. Results and discussion

3.1 Chemical composition analysis

Fig. 2 illustrates XRD patterns of ZrO_2-SiO_2 coatings sintered at 1100 °C for 2 h with various SiO_2 contents. As shown, the coatings have monoclinic crystalline structure. The monoclinic ZrO_2 is often preferred in biomedical applications [41, 42], because hydroxyapatite (HA) can form easily on this crystallographic structure due to easily formation of tri-bridging hydroxyl groups during immersion in biological media [43]. The SiO_2 phase was not detected in XRD patterns (Fig. 2), indicating its amorphous structure. The same result has been reported for HA-SiO_2 composite coating [44]. In biological applications, the evidence of zircon ($ZrSiO_4$) degrades the performance of ZrO_2-SiO_2 coatings. According to ZrO_2-SiO_2 phase diagram, zircon is formed through solid state reaction between ZrO_2 and SiO_2 approximately beyond 1000 °C in ZrO_2-SiO_2 binary oxide system with SiO_2 molar ratio lower than 50 mol. % [45]. Based on XRD results in Fig. 2, zircon is not detected after 2 h sintering of the coated samples at 1100 ^oC. Similarly, Monte *et al.* [46] have reported no zircon formation in ZrO_2-SiO_2 composite even after sintering at 1200 °C for 6 h. This retarding in zircon formation has been explained well in ref. [47] and is related to the presence of carbonadoes impurities

coming from the alkoxide precursors, which probably accumulate in the grain boundaries, acting as an effective diffusion barrier [47].

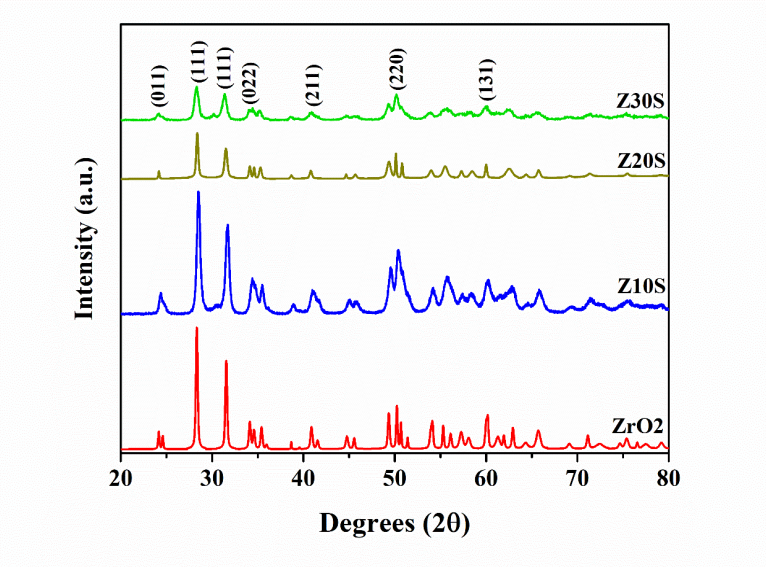

Fig. 2. XRD patterns of ZrO_2-SiO_2 coatings on anodic oxidized surface of 316L substrate sintered at 1100 °C for 2 h.

Crystallite size of coatings was calculated from the XRD patterns using Debye Scherrer equation [48], and found to be 29, 26, 15 and 13 nm for ZrO_2, Z10S, Z20S and Z30S coatings, respectively. Although diffraction patterns of ZrO_2 and Z10S samples are almost similar, they look different for Z20S and Z30S samples. In fact, the diffraction peaks broaden with increasing SiO_2 content, indicating smaller crystallite sizes formation. This is known as "constrained effect", in which, zirconia nuclei are surrounded by a shell of amorphous silica and inhibited to grow [49]. The constrained effect is intensified by increasing the silica content.

3.2 Surface morphology and interface structure of coatings

Fig. 3 shows surface morphology of the coatings sintered at 1100 and 1150 °C for 2 h. As seen, surface topography of coatings and crack density are strongly affected by SiO_2 content. In low-magnification SEM images given in Figs. $3a_1$-d_1, it appears that the coatings with no

cracks and free of defects are achieved following sintering at 1100 °C. The ZrO_2 coating revealed a rough surface with a wavy-like structure similar to the bioactive glass coatings produced on 316L substrate using EPD at high DC voltage (90 V) [50]. However, by introducing amorphous SiO_2 into ZrO_2 structure, surface of the coatings became more uniform and the most homogeneity was achieved for Z30S sample (Fig. $3d_1$). All coatings consisted of submicron particles with no coarse agglomerates on the surface, revealing a packed structure. As it is obvious from Fig. $3d_2$, Z30S particles showed the best sintering behavior by forming a closely packed structure without large voids.

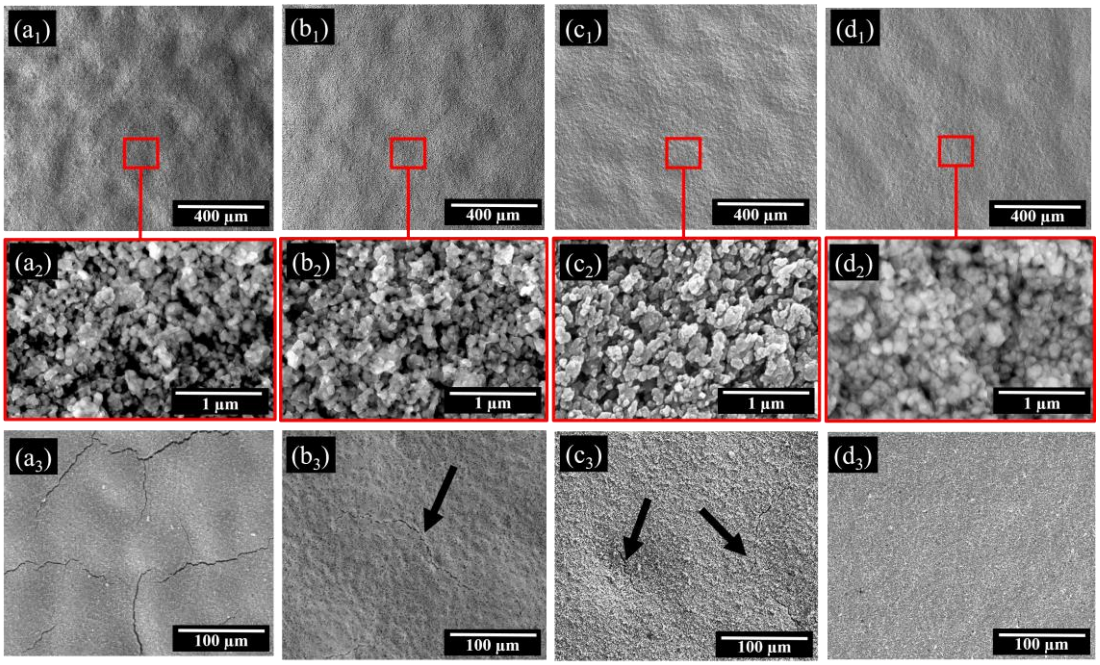

Fig. 3. SEM images of coatings sintered with heating rate of 2 °C/min for 2 h in vacuum furnace under pressure of 10^{-5} torr at 1100 °C: (a_1, a_2) ZrO_2, (b_1, b_2) Z10S, (c_1, c_2) Z20S and (d_1, d_2) Z30S and 1150 °C: (a_3) ZrO_2, (b_3) Z10S, (c_3) Z20S and (d_3) Z30S

By increasing the sintering temperature to 1150 °C, intensive cracking due to coating shrinkage is observed for ZrO_2 coating resulting from the difference in coefficient of thermal expansion (CTE) between coating and 316L substrate [55] (Fig. $3a_3$). However, the possibility of cracking is reduced for Z10S and Z20S coatings, although some small micro-cracks are still present on their surface (Fig. $3b_3$-c_3, black arrows). By further increasing the

SiO_2 content, cracks were varnished and a smooth and defect-free surface is achieved for Z30S sample (Fig. 3d3). During sintering, ceramic coatings usually shrink and tensile stresses are developed, which are relieved by crack formation [17]. Introducing amorphous silica into ZrO_2 structure has hindered stress-induced cracking, indicating efficient sintering properties of ZrO_2-SiO_2 particles containing appropriate SiO_2 content (e.g. 30 mol. % SiO_2).

Porosity of coatings produced using EPD process can be influenced strongly by particles morphology [51], particles size [52] and electrophoretic mobility [53]. As particles used in this study have irregular shapes (Fig. 4a-d), the porosity is not influenced by particles morphology. As shown in Fig. 4e, the mean particle size, determined by ImageJ software, decreases with increasing SiO_2 content. As fine particles provide high effective surface area, they create dense deposits with packed arrangement which ultimately leads to minimize coating cracking [54].

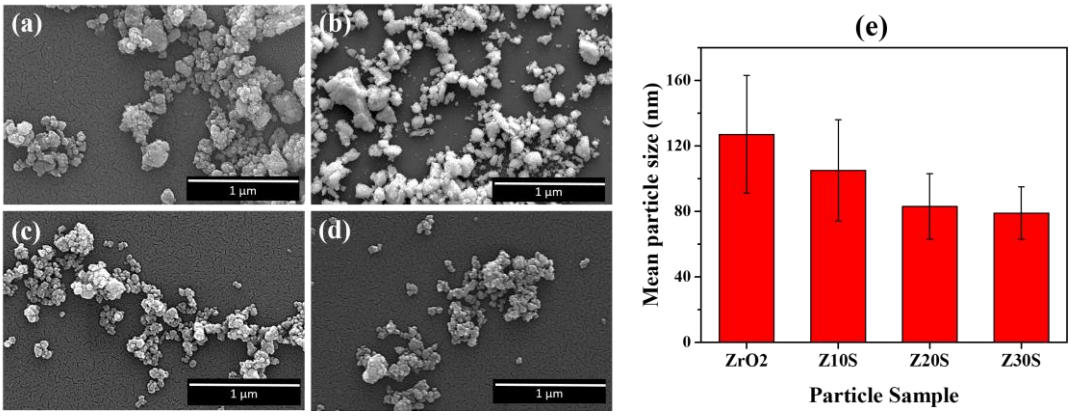

Fig. 4. SEM images of particles: a) ZrO_2, b) Z10S, c) Z20S and d) Z30S; and e) mean size of the particles.

According to Fig. 5, Z30S particles with the lowest size show the highest zeta potential and thus the highest electrophoretic mobility and suspension stability [55], resulting in a denser coating (Fig. 3d2). As seen, the coating densification is under the influence of intrinsic chemical composition of particles, which consecutively, affects the particles' size and zeta potential. In fact, integration of amorphous silica into ZrO_2 structure facilitates atomic surface diffusion at the interface of attached particles at elevated temperatures [46]. For this reason,

silica facilitates the sintering process and refines the coating porosity through building up strong chemical bonding between the particles. In this way, Z30S coating possesses the highest packing structure.

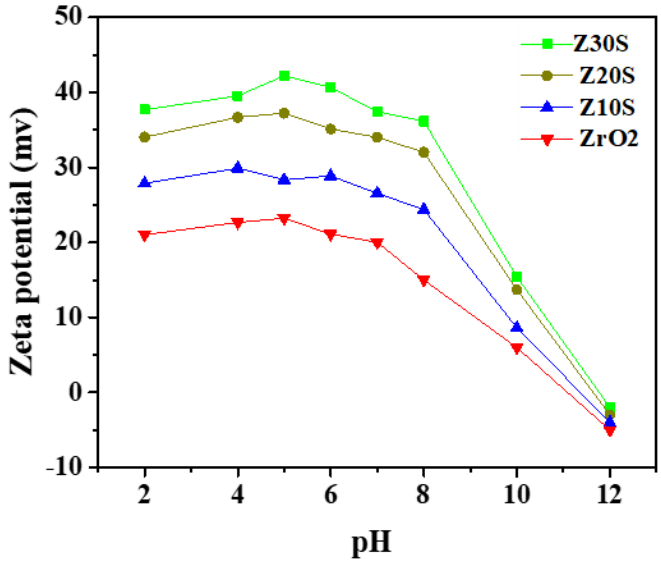

Fig. 5. Zeta potential of ZrO_2 and ZrO_2-SiO_2 composite particles as a function of pH.

To evaluate the influence of SiO_2 content on the interaction of particles with anodic oxidized surface of 316L stainless steel substrate, SEM cross sectional images were provided from coatings sintered at 1100 °C (Fig. 6). As is seen, a dense interlayer is formed at the coating/substrate interface of all samples. The interlayer thickness increased with the increase of SiO_2 content and was measured 0.34, 0.60, 1.11 and 1.15 µm for ZrO_2, Z10S, Z20S and Z30S coatings, respectively. This is because of a more facile incorporation of ZrO_2-SiO_2 particles containing higher silica into the porous anodic oxide layer due to the higher atomic surface diffusion supported by silica at the interface of attached particles as discussed before. This indicates the crucial role of silica in interlayer formation. The dense interlayer formed here is very similar to those intermediate layers developed by plasma electrolytic oxidation (PEO) on metals such as Al [56], Mg [57] and Ti [58]. However, the accessible thickness of compact interlayers created by PEO method [59] is significantly higher than these obtained in our study.

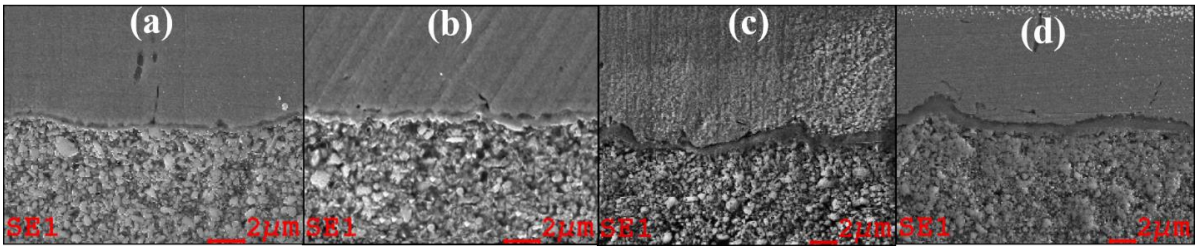

Fig. 6. Cross-sectional SEM images from interface of (a) ZrO_2, (b) Z10S, (c) Z20S and (d) Z30S coatings sintered at 1100 °C.

EDS elemental mapping was performed for further analysis of chemical composition of newly formed interlayers. As seen in Fig. 7, for all coatings, the interlayer is mainly enriched by Cr, Mn and O elements, and therefore, it probably consists of chromium and manganese mixed oxides. In addition, as seen from Figs. 7c and d, Ni has also diffused from substrate into the interlayer region of Z20S and Z30S coatings, evidenced as parallel bonds at the coating/substrate interface (marked in Fig. 7c and d). The thickness of Ni-rich bond is higher for Z30S coating, indicating that the interfacial diffusion is facilitated by raising the silica content. Thus, the interlayer is enriched by more diffused elements especially in Z30S coating, which can also be another reason for its higher thickness.

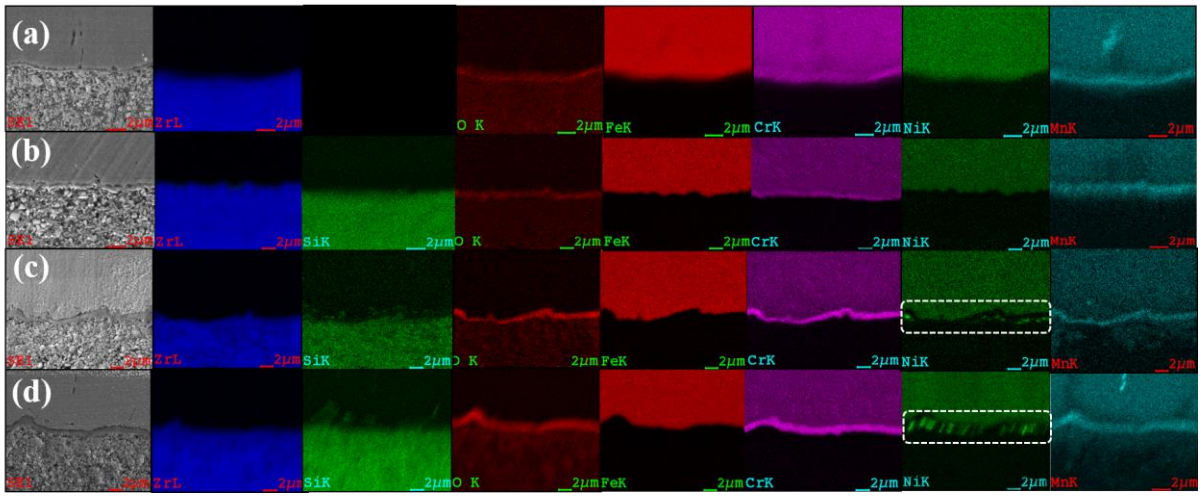

Fig. 7. EDS elemental mapping of: (a) ZrO_2, (b) Z10S, (c) Z20S, and (d) Z30S coatings sintered at 1100 °C.

3.3 FIB tomography of coatings

In order to reconstruct actual pore structure of coatings using FIB tomography, the captured SEM image resolution of each slice needs to be more than the minimum dimensions of pore volume existing inside the ROI area. The voxel volume, representing the resolution in three dimensions, is the volume that a new 3D image can be reconstructed by repeating in x, y and z dimensions [60]. The dimension in z direction is the thickness of each slice, considered 50 nm in this study (Fig. 1b); the x and y dimensions are based on the pixel sizes of SEM images, pixel resolution, and both of them are considered 50 nm. Therefore, minimum detectable pore volume, known as voxel resolution, and equivalent pore diameter are approximately 1.25×10^{-4} μm^3 and 50 nm, respectively.

3D reconstructed images from ROI of the deposited coatings sintered at 1100 ^{o}C are presented in Fig. 8. These images consist of particles firmly attached together during the sintering process which reveal a pore network including connected and isolated pores. Other defects such as internal cracks were not detected for coated samples, designating on a homogeneous crack-free porous structure through cross section of the coatings. As seen from Fig. 8, by increasing the SiO_2 content, the volume fraction of isolated pores increases at the expense of connected pores. In this regards, ZrO_2 coating reveals the highest volume fraction of connected pores (Fig. 8a), while the lowest one is obtained for Z30S sample (Fig. 8d). However, the volume fraction of connected pores is almost the same for Z10S and Z20S coatings, which is clear from red color sub-reconstructed 3D images (Figs. 8b and c). To explore precise statistical information and classify the connected and isolated pores, quantitative analysis is conducted and the results are summarized in Table 1.

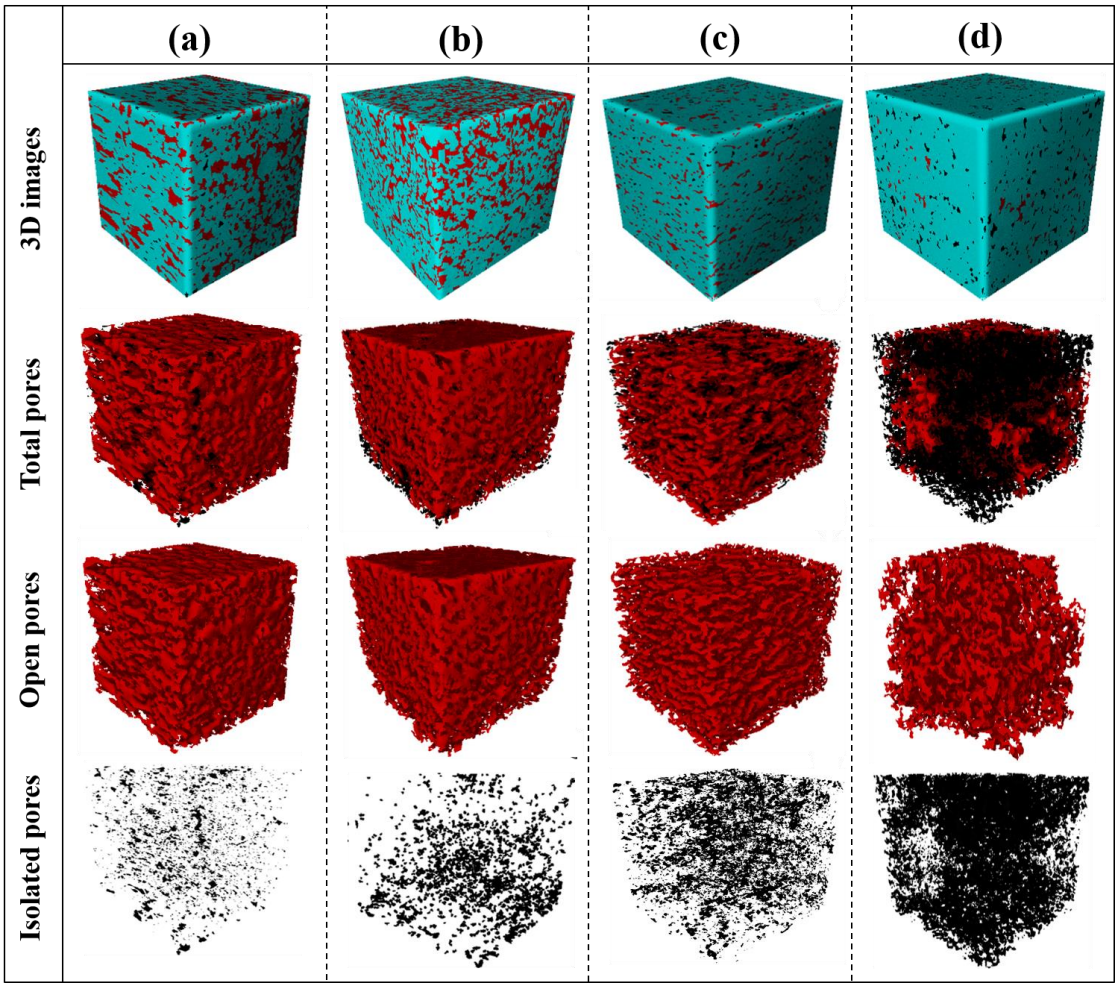

Fig. 8. 3D reconstructed and sub-reconstructed images of: (a) ZrO_2, (b) Z10S, (c) Z20S and (d) Z30S coatings.

(●: particles, ●: connected pores, ●: isolated pores)

Table 1. Volume percent of pores distribution for ZrO_2-xSiO_2 coatings (x=0, 10, 20, 30)

Sample Code	Volume (μm³)			
	ROI	Total pores	Connected pores	Isolated pores
ZrO_2	3375	953.77 (28.27 %)	931.51 (27.61 %)	22.28 (0.66 %)
Z10S	3375	764.45 (22.68 %)	681.75 (20.23 %)	82.68 (2.45 %)
Z20S	3375	490.39 (14.53 %)	384.08 (11.38 %)	106.31 (3.15 %)
Z30S	3375	392.51 (11.63 %)	209.59 (6.21 %)	182.93 (5.42 %)

It was found that the total pores volume of Z30S coating (392.51 μm^3) has decreased ~ 2.43 times in comparison with ZrO_2 sample (953.77 μm^3). In addition, the portion of isolated pores in ZrO_2 coating was only 0.66 % of total pore volume, while this value increased to

5.42 % for Z30S coating. Furthermore, the highest compact structure was obtained for Z30S coating indicating that the silica acts as a pores refining component. This finding can open a new approach for fabrication of future ceramic coatings with tailored porosity through combination of various amorphous and crystalline structures of ceramic materials. Here, the pore refining effect of SiO_2 is in agreement with the results obtained for PEO coating produced on 6061 Al, where the incorporation of SiO_2 nanoparticles provides higher compact coatings [61]. In another example, adding 4 and 20 wt. % SiO_2 nanoparticles considerably reduced the porosity of ZrO_2-calcium phosphate coating from 54 % down to 7 % and 1 %, respectively, after sintering at 1200 ^oC [62]. Using FIB-tomography technique, Lim *et al.* [63] have shown that nano-silica particles have refined the pore structure of cement paste materials and improved the durability. They concluded that the total porosity and also pore diameter decrease with entering the nano-silica into the cement paste structure, indicating that it acts as a suitable pores filler component. Fig. 9 displays the porosity values obtained using tomography technique.

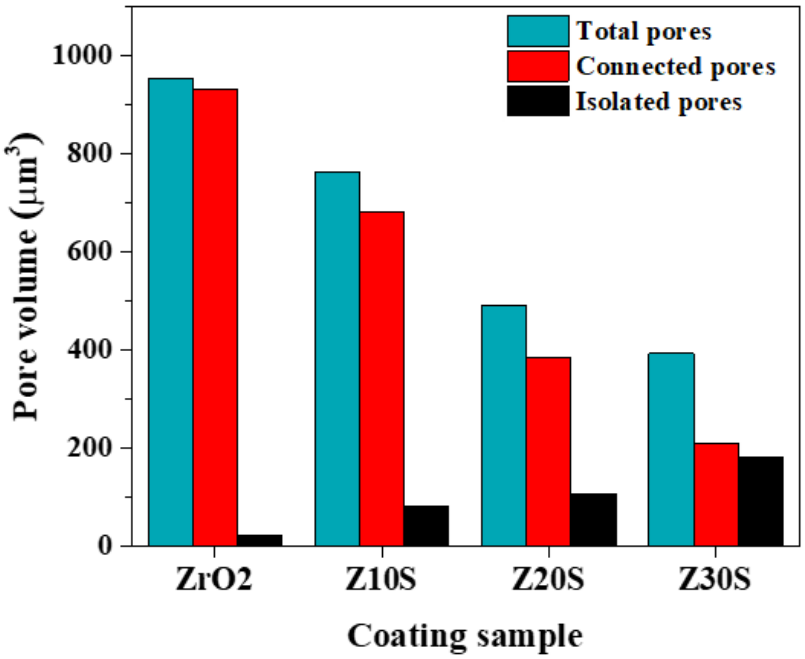

Fig. 9. Pore volume of various type of porosities (total, connected and isolated pores) calculated from tomography technique as a function of coating composition.

To investigate shape, volume and size of the isolated pores, 3D sub-reconstructed images along with related volume histograms were extracted and shown in Fig 10. The volume histogram describes the frequency of volume size distribution of isolated pores inside the ROI area. The ZrO_2 coating revealed the narrowest distribution as well as the smallest isolated pore size among the coatings (Fig. 10a). However, the volume distribution of isolated pores in Z10S coating (Fig. 10b) was raised to 0.25 μm^3, approximately three times higher than that of ZrO_2 coating (0.075 μm^3). The volume and also distribution of isolated pores remain almost unchanged with further increasing the SiO_2 content, i.e. Z20S sample (Fig. 10c). As seen in Fig. 10d, the volume percent of isolated pores in Z30S coating (5.42 %) was suddenly increased ~ 14 times relative to that of ZrO_2 coating (0.66 %) and ~ 4 times compared with Z10S and Z20S ones. The Z30S coating contained isolated pores with volume size less than ~ 1 μm^3; however, some larger pores showing volume size of 1.5 μm^3 and even 3.5 μm^3 were distributed at the edge of 3D image with lower frequencies (Fig. 8d). Clearly, some parts inside the 3D sub-reconstructed image were locally free of the isolated pores resulted by firm attachment of particles, indicating inhomogeneous distribution of the isolated pores in Z30S coating. The isolated pores for all coatings have irregular and complicated shapes, which become larger and more complex in Z30S coating.

As seen from 3D images in Fig. 8, connected pores consist of channels irregularly interconnected to each other leading to the formation of undefined and puzzled routes. As seen in Table 1, volume percent of the connected pores was reduced by increasing the silica content of coating, as the least value (6.21 %) was obtained for the Z30S coating compared with 27.61 % for ZrO_2 coating. Fig. 11 represents the size distribution histogram of the connected pores for all coatings. As it is seen, the equivalent diameter of pores also decreased with increasing the SiO_2 content. Decreasing of both volume percent and size of connected pores indicate a restriction on path-through channels of coating permitting the diffusion of

corrosive solution. However, it should be remarked that dimension of the connected pores contacting with living tissues, i.e. surface connected pores, is the important contributing factor that influences the bioactive properties of the coated surface [8, 64]. It has been reported that the nano-porous structure (i.e. pore size < 100 nm [65]) can accelerate HA formation (bioactivity) and enhance osteoblast function [66, 67]. On the other hand, microporous structure (pore size < 10 μm [68]) improves bone ingrowth and mechanical fixation of bone to the implant [69]. Clearly, all coatings show a microporous structure (Fig. 11) confirming their potential applications for improving bone fixation and reduction of stress shield effect.

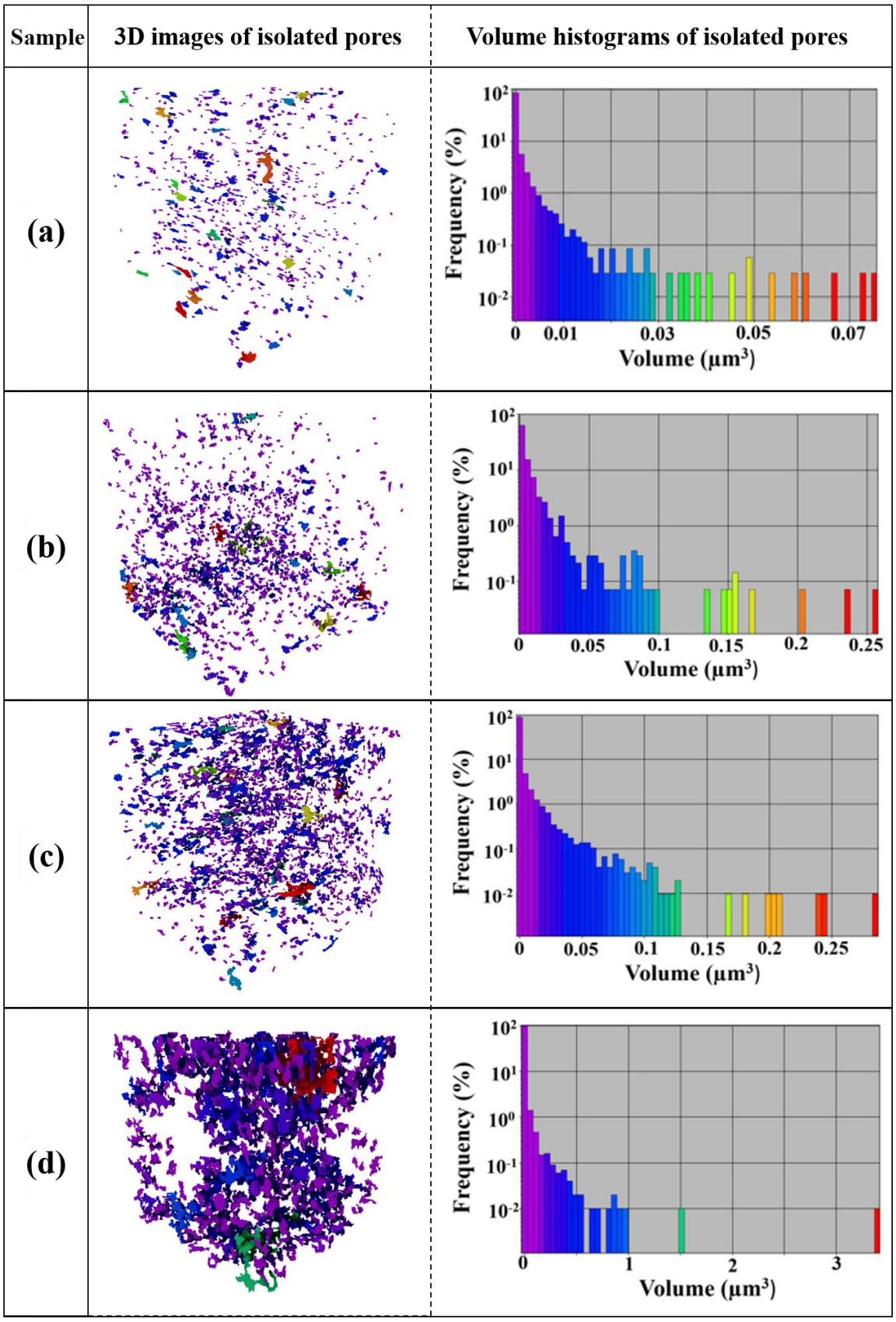

Fig. 10. 3D sub-reconstructed images and volume histograms of isolated pores of: (a) ZrO_2, (b) Z10S, (c) Z20S and (d) Z30S coatings.

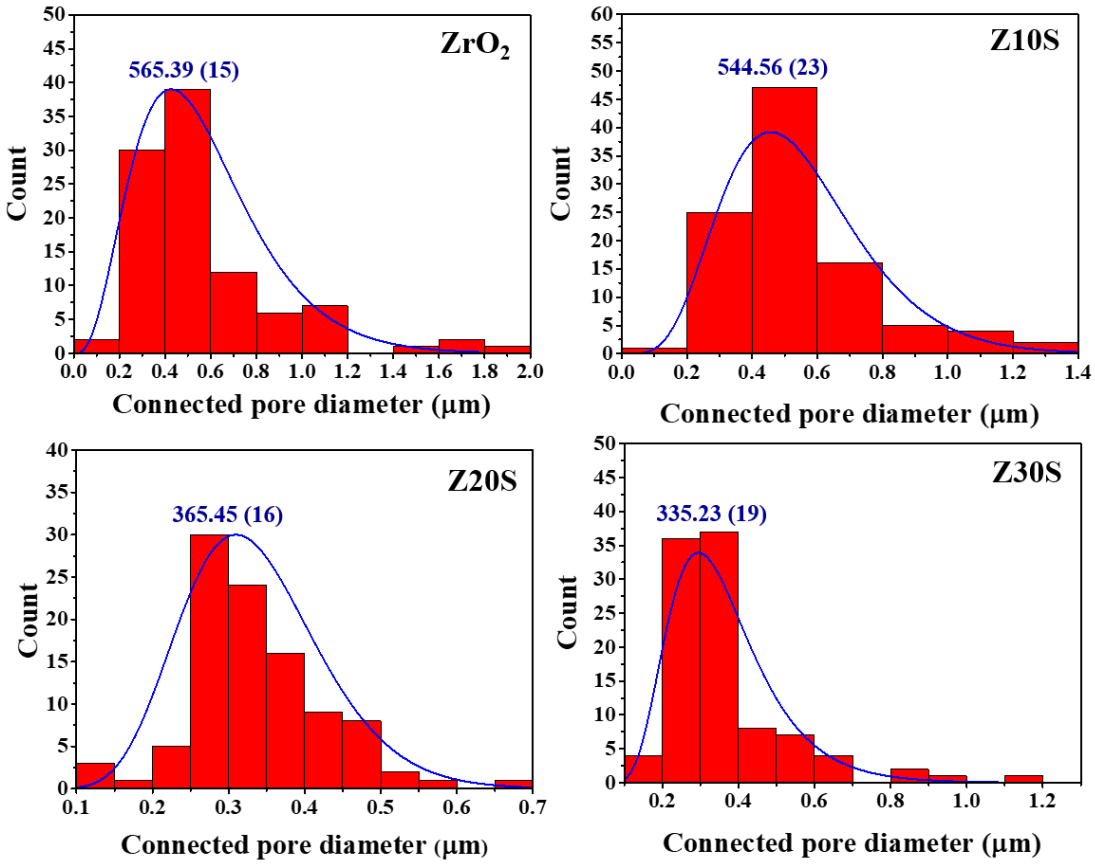

Fig. 11. Size distribution histogram of connected pores along with the average equivalent diameter for various coated samples.

3.4 Corrosion behavior of coated samples

Fig. 12 illustrates the potentiodynamic polarization plots of uncoated anodic oxidized 316L substrate and coated samples sintered at 1100 °C for 2 h in an SBF solution for 24 h at 37 °C. All curves display a passive behavior. By applying ZrO_2 coating, significant lower current values can be observed demonstrating its good barrier properties. By adding and increasing the SiO_2 content, more shift in polarization curves to the lower current densities and also more positive potentials were seen, indicating that ZrO_2-SiO_2 composite coatings provide higher barrier effect than ZrO_2 coating. As seen, Z30S sample demonstrates the lowest passive current density and the most noble corrosion potential. Moreover, the passive region of uncoated substrate is relatively narrow; while, it extends for the coated samples and

reaches to a maximum value for Z30S sample. This is believed to be due to its capability to form a more dense interlayer through the sintering process. According to ref. [70], ZrO_2-50 mol. % SiO_2 composite coating produced on 316L substrate exhibited a significant improvement in corrosion performance compared with ZrO_2, SiO_2 and ZrO_2-70 mol. % SiO_2 composite coating.

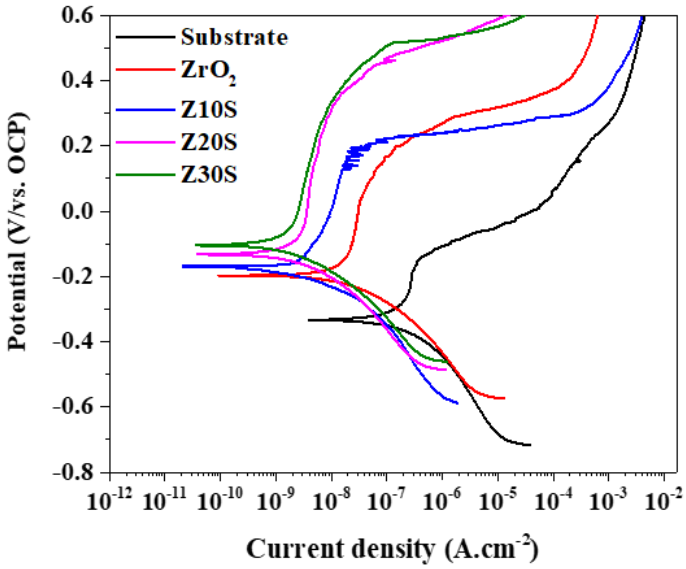

Fig. 12. Potentiodynamic polarization plots drawn after 24 h immersion in SBF solution at 37 °C.

The obvious inflection on anodic branch of polarization curves shows breakdown potential representing the start of localized attack. The 316L substrate shows the lowest value of breakdown potential owing to the presence of numerous defects and pores introduced by anodic oxidation treatment. The breakdown potential is significantly shifted toward a nobler potential when ZrO_2 coating is applied on the substrate and remains almost constant for Z10S coated sample. On the other hand, Z30S coated sample reveals the highest value of breakdown potential, resulted by its lower porosity and higher thickness of interlayer.

In order to further evaluate the corrosion performance of samples, electrochemical impedance spectroscopy (EIS) was performed at OCP in the same condition as potentiodynamic polarization tests. Fig. 13a illustrates Nyquist plots of experimental and simulated data of

coated samples. The Nyquist curve related to ZrO_2 coated sample shows an incomplete capacitive behavior, representing the passivation behavior. According to the Bode-phase curve (Fig. 13b), two distinct humps close to 1 Hz and 1 kHz indicating two time constants are present for ZrO_2 sample. For ZrO_2-SiO_2 composite coatings, the humps are somewhat merged to appear as a semi-plateaus and lie at higher phase angles with increasing SiO_2 content, denoting a more effective barrier behavior. The barrier effect is more dominantly provided by the interlayer created through sintering process. Increasing the silica content of coating intensifies the interlayer thickness which subsequently improves the barrier effect of the coating. The interlayer thickness is the highest for Z30S sample, and thus, it reveals the highest corrosion performance. In our previous study [71], it was found that the interlayer was formed by integration of ZrO_2-SiO_2 particles with anodic oxide layer at upper parts of the substrate surface porosities. For Z30S sample, the minimum volume percent of connected pores (6.21 % based on tomography results) represents its resistance against entering of aggressive solution inside the coating.

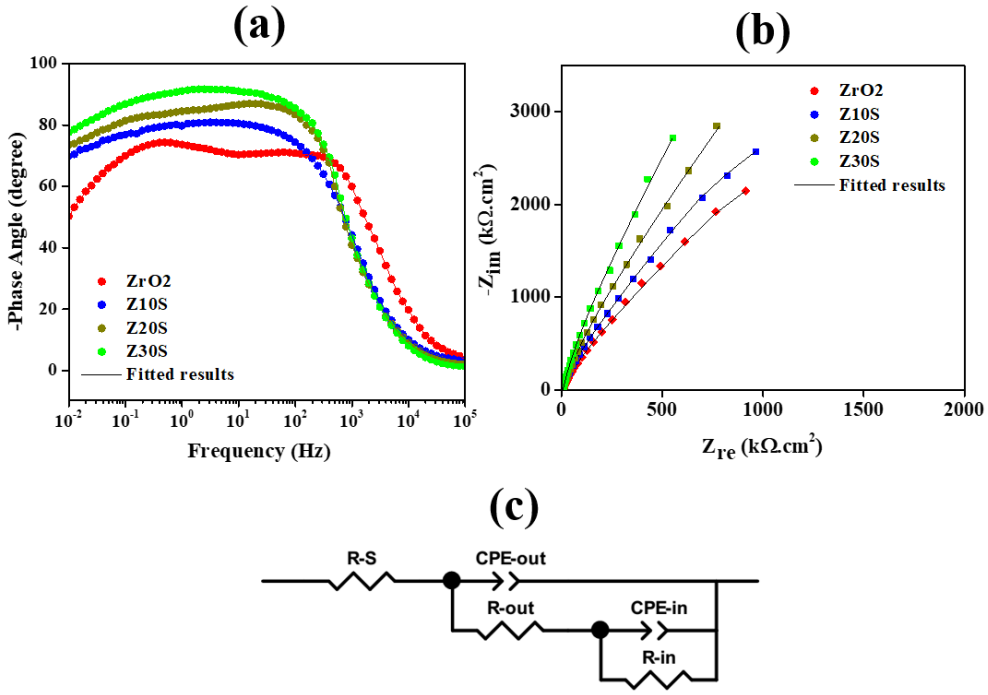

Fig. 13. (a) Nyquist, (b) Bode-phase plots from ZrO_2-SiO_2 coated samples after 24 h immersion in SBF at 37 ^oC and (c) EC model applied for fitting impedance.

An equivalent electrical circuit (EC) with two-layer structure dielectric (inner compact layer and outer porous layer) is applied for fitting the experimental data using the Z-view software and the extracted impedance data are summarized in Table 3. As seen in Fig. 13c, the proposed EC model consists of R_s, (R_{in}-CPE_{in}) and (R_{out}-CPE_{out}) combinations. The R_s represents the uncompensated solution resistance, (R_{in}-CPE_{in}) which accounts for the low-frequency time constant mostly raised by the interlayer and (R_{out}-CPE_{out}) refers to the high-frequency time constant corresponding to the bulk coating effect. The constant phase element (CPE) is used instead of pure capacitance (C) because of non-ideal capacitive behavior, which is explained by several reasons such as microscopic surface roughness, surface defects and heterogeneity at the interfaces [72]. Moreover, total coating resistance (R_t) is considered as sum of the inner and outer resistances, (R_{in} + R_{out}), showing the highest value for Z30S. R_{in} of coatings stems mostly from dense interlayer with a value proportional to its thickness; while, R_{out} is responded from porous structure of coating body in coincidence with the volume fraction of connected pores. As is seen, R_{in} is significantly higher than R_{out} for all coated samples indicating that the overall corrosion performance of the coatings is mostly determined by the barrier effect of interlayer.

Table 2. Electrical elements extracted by fitting EIS data using EC in Fig. 13c

Sample Code	**CPE_{in} ($\mu F.cm^{-2}.s^{n-1}$)**	**n_{in}**	**R_{in} ($M\Omega.cm^2$)**	**CPE_{out} ($\mu F.cm^{-2}.s^{n-1}$)**	**n_{out}**	**R_{out} ($\Omega.cm^2$)**
ZrO_2	0.15 (0.02)	0.89 (0.02)	101.42 (8.21)	1.34 (0.08)	0.89 (0.02)	498.13 (15.31)
Z10S	0.10 (0.01)	0.73 (0.03)	133.00 (12.18)	0.59 (0.05)	0.81 (0.03)	657.00 (19.76)
Z20S	0.08 (0.02)	0.69 (0.03)	157.27 (11.18)	0.41 (0.01)	0.75 (0.01)	822.12 (17.41)
Z30S	0.07 (0.01)	0.64 (0.01)	183.84 (10.31)	0.37 (0.03)	0.72 (0.03)	931.75 (15.35)

Fig. 14 illustrates variation of R_{out} values and volume percent of connected pores obtained from 3D FIB-tomography, as a function of coating composition. Clearly, the R_{out} values are inversely proportional to the percent of connected pores indicating a correlation between electrochemical impedance response and the coatings microstructure. The maximum value of

R_{out} (931.75 Ω.cm^2) is obtained for Z30S coated sample with 6.21 % volume of connected pores, which is the least value compared to other coated samples. Moreover, this sample shows the most thickness of dense interlayer. For these two reasons, it could be expected that the Z30S coated sample presents the best barrier performance along with the less permeability against corrosive solution, leading to the most corrosion performance.

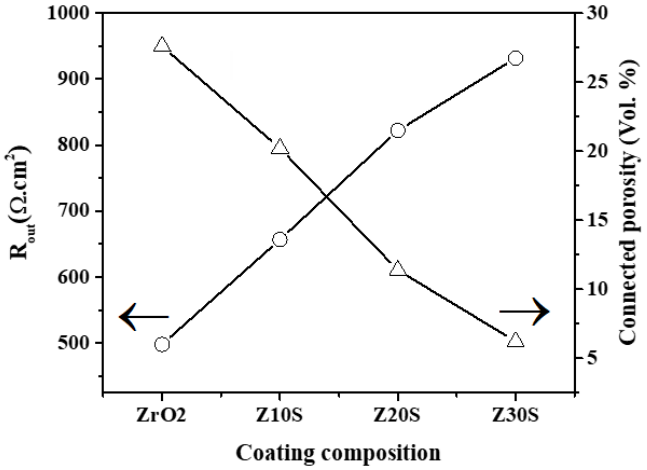

Fig. 14. Variation of R_{out} values and volume percent of connected pores as a function of coating composition.

4. Conclusions

Incorporation of amorphous SiO_2 into the ZrO_2 structure hindered crack propagation in ZrO_2-SiO_2 composite coatings and also increased thickness of the dense interlayer formed at the coating/substrate interface. Based on 3D-FIB tomography results, the coating with the highest SiO_2 content (i.e. ZrO_2-30 mol. % SiO_2) represented highly packed structure with the lowest volume percent of total porosity (11.6 %) as compared with ZrO_2 coating (28.27 %). Furthermore, volume percent of isolated pores increased at expense of connected pores with increasing SiO_2 content. Equivalent diameter of connected pores was also decreased by increasing the SiO_2 content. However, all coatings contained macro-porous structures indicating that these coatings can improve bone ingrowth and mechanical fixation. Correlation between corrosion performance and tomography results indicated that the outer layer resistance of coatings was inversely proportional to the volume percent of connected

pores, while the inner layer resistance of coatings was responded by the interlayer. Corrosion performance of ZrO_2-SiO_2 coatings was improved with increasing SiO_2 content, due to the higher barrier effect resulted by increasing the interlayer thickness as well as the lower permeability against aggressive solution created by the lower amount of connected pores.

Conflict of interests

The authors declare that they have no conflict of interests.

Acknowledgment

The authors would like to acknowledge the financial support by the Research Council of Norway through the HyF-Lex (244068/E30) project. The Research Council of Norway is acknowledged for support to NTNU NanoLab through the Norwegian Micro- and Nano-Fabrication Facility, Norfab (197411/V30).

References

[1] A.R. Studart, U.T. Gonzenbach, E. Tervoort, L.J. Gauckler, Processing routes to macroporous ceramics: a review, J. Am. Ceram. Soc., 89 (2006) 1771-1789 https://doi.org/1710.1111/j.1551-2916.2006.01044.x.
[2] R.T. Candidato Jr, R. Sergi, J. Jouin, O. Noguera, L. Pawłowski, Advanced microstructural study of solution precursor plasma sprayed Zn doped hydroxyapatite coatings, J. Eur. Ceram. Soc., 38 (2018) 2134-2144 https://doi.org/2110.1016/j.jeurceramsoc.2017.2112.2037.
[3] D. Stojanovic, B. Jokic, D. Veljovic, R. Petrovic, P. Uskokovic, D. Janackovic, Bioactive glass–apatite composite coating for titanium implant synthesized by electrophoretic deposition, J. Eur. Ceram. Soc., 27 (2007) 1595-1599 https://doi.org/1510.1016/j.jeurceramsoc.2006.1504.1111.
[4] X. Gu, N. Li, W. Zhou, Y. Zheng, X. Zhao, Q. Cai, L. Ruan, Corrosion resistance and surface biocompatibility of a microarc oxidation coating on a Mg–Ca alloy, Acta Biomater., 7 (2011) 1880-1889 https://doi.org/1810.1016/j.actbio.2010.1811.1034.
[5] T.H. Qaid, S. Ramesh, F. Yusof, W.J. Basirun, Y.C. Ching, H. Chandran, S. Ramesh, S. Krishnasamy, Micro-arc oxidation of bioceramic coatings containing eggshell-derived hydroxyapatite on titanium substrate, Ceram. Int., 45 (2019) 18371-18381 https://doi.org/18310.11016/j.ceramint.12019.18306.18052.
[6] S.A. Adeleke, S. Ramesh, A.R. Bushroa, Y.C. Ching, I. Sopyan, M.A. Maleque, S. Krishnasamy, H. Chandran, H. Misran, U. Sutharsini, The properties of hydroxyapatite ceramic coatings produced by plasma electrolytic oxidation, Ceram. Int., 44 (2018) 1802-1811 https://doi.org/1810.1016/j.ceramint.2017.1810.1114.
[7] M. Farrokhi-Rad, S.K. Loghmani, T. Shahrabi, S. Khanmohammadi, Electrophoretic deposition of hydroxyapatite nanostructured coatings with controlled porosity, J. Eur. Ceram. Soc., 34 (2014) 97-106 https://doi.org/110.1016/j.jeurceramsoc.2013.1007.1022.
[8] S. Roedel, J.C.M. Souza, F.S. Silva, J. Mesquita-Guimarães, M.C. Fredel, B. Henriques, Optimized route for the production of zirconia structures with controlled surface porosity for biomedical applications, Ceram. Int., 44 (2018) 12496-12503 https://doi.org/12410.11016/j.ceramint.12018.12404.12042.

[9] A. Portinha, V. Teixeira, J. Carneiro, J. Martins, M. Costa, R. Vassen, D. Stoever, Characterization of thermal barrier coatings with a gradient in porosity, Surf. Coat. Technol., 195 (2005) 245-251 https://doi.org/210.1016/j.surfcoat.2004.1007.1094.
[10] X. Miao, D. Sun, Graded/gradient porous biomaterials, Materials, 3 (2010) 26-47 https://doi.org/10.3390/ma3010026.
[11] B. Henriques, D. Fabris, J.C. Souza, F.S. Silva, J. Mesquita-Guimarães, Y. Zhang, M. Fredel, Influence of interlayer design on residual thermal stresses in trilayered and graded all-ceramic restorations, Mater. Sci. Eng. C, 71 (2017) 1037-1045 https://doi.org/1010.1016/j.msec.2016.1011.1087.
[12] A. Bandyopadhyay, F. Espana, V.K. Balla, S. Bose, Y. Ohgami, N.M. Davies, Influence of porosity on mechanical properties and in vivo response of Ti6Al4V implants, Acta Biomater., 6 (2010) 1640-1648 https://doi.org/1610.1016/j.actbio.2009.1611.1011.
[13] D.N. Boccaccini, H.L. Frandsen, S. Soprani, M. Cannio, T. Klemensø, V. Gil, P.V. Hendriksen, Influence of porosity on mechanical properties of tetragonal stabilized zirconia, J. Eur. Ceram. Soc., 38 (2018) 1720-1735 https://doi.org/1710.1016/j.jeurceramsoc.2017.1709.1029.
[14] M. Garcia-Lobato, A. Mtz-Enriquez, C. Garcia, M. Velazquez-Manzanares, F. Avalos-Belmontes, R. Ramos-Gonzalez, L. Garcia-Cerda, Corrosion resistance and in vitro bioactivity of dense and porous titania coatings deposited on 316L SS by spraying method, Appl. Surf. Sci., 484 (2019) 975-980 https://doi.org/910.1016/j.apsusc.2019.1004.1108.
[15] L. Qiao, Y. Wu, S. Hong, J. Cheng, Z. Wei, Influence of the high-velocity oxygen-fuel spray parameters on the porosity and corrosion resistance of iron-based amorphous coatings, Surf. Coat. Technol., 366 (2019) 296-302 https://doi.org/210.1016/j.surfcoat.2019.1003.1046.
[16] E.C. Hammel, O.L.R. Ighodaro, O.I. Okoli, Processing and properties of advanced porous ceramics: An application based review, Ceram. Int., 40 (2014) 15351-15370 https://doi.org/15310.11016/j.ceramint.12014.15306.15095.
[17] P. Sarkar, P.S. Nicholson, Electrophoretic deposition (EPD): mechanisms, kinetics, and application to ceramics, J. Am. Ceram. Soc., 79 (1996) 1987-2002 https://doi.org/1910.1111/j.1151-2916.1996.tb08929.x.
[18] S. Cabanas-Polo, A.R. Boccaccini, Electrophoretic deposition of nanoscale TiO_2: technology and applications, J. Eur. Ceram. Soc., 36 (2016) 265-283 https://doi.org/210.1016/j.jeurceramsoc.2015.1005.1030.
[19] I. Narkevica, L. Stradina, L. Stipniece, E. Jakobsons, J. Ozolins, Electrophoretic deposition of nanocrystalline TiO_2 particles on porous TiO_2-x ceramic scaffolds for biomedical applications, J. Eur. Ceram. Soc., 37 (2017) 3185-3193 https://doi.org/3110.1016/j.jeurceramsoc.2017.3103.3053.
[20] K. Moritz, T. Moritz, ZrO_2 ceramics with aligned pore structure by EPD and their characterisation by X-ray computed tomography, J. Eur. Ceram. Soc., 30 (2010) 1203-1209 https://doi.org/1210.1016/j.jeurceramsoc.2009.1205.1034.
[21] A.V. Kerkar, Manufacture of conical pore ceramics by electrophoretic deposition, US Patent 5 472 583, 1995; EP 0589 548 A1, 1994.
[22] J.-i. Hamagami, Y. Ato, K. Kanamura, Fabrication of highly ordered macroporous apatite coating onto titanium by electrophoretic deposition method, Solid State Ion., 172 (2004) 331-334 https://doi.org/310.1016/j.ssi.2004.1002.1046.
[23] D. Mochizuki, R. Tanaka, S. Makino, Y. Ayato, W. Sugimoto, Vertically Aligned Reduced Graphite Oxide Nanosheet Film and its Application in a High-Speed Charge/Discharge Electrochemical Capacitor, ACS Appl. Energy Mater., 2 (2019) 1033-1039 https://doi.org/1010.1021/acsaem.1038b01478.
[24] I. Avramova, D. Stoychev, T. Marinova, Characterization of a thin CeO_2–ZrO_2–Y_2O_3 films electrochemical deposited on stainless steel, Appl. Surf. Sci., 253 (2006) 1365-1370 https://doi.org/1310.1016/j.apsusc.2006.1302.1011.
[25] S.M.A. Shibli, F. Chacko, C. Divya, Al_2O_3–ZrO_2 mixed oxide composite incorporated aluminium rich zinc coatings for high wear resistance, Corros. Sci., 52 (2010) 518-525 https://doi.org/510.1016/j.corsci.2009.1010.1008.
[26] K.Y. Jung, S.B. Park, Photoactivity of SiO_2/TiO_2 and ZrO_2/TiO_2 mixed oxides prepared by sol–gel method, Mater. Lett., 58 (2004) 2897-2900 https://doi.org/2810.1016/j.matlet.2004.2805.2015.
[27] M. Poorraeisi, A. Afshar, Synthesizing and comparing HA–TiO_2 and HA–ZrO_2 nanocomposite coatings on 316 stainless steel, SN Appl. Surf., 1 (2019) 155 https://doi.org/110.1007/s42452-42019-40168-42452.
[28] J. Curran, T. Clyne, Porosity in plasma electrolytic oxide coatings, Acta Mater., 54 (2006) 1985-1993 https://doi.org/1910.1016/j.actamat.2005.1912.1029.
[29] F. Sondej, A. Bück, K. Koslowsky, P. Bachmann, M. Jacob, E. Tsotsas, Investigation of coating layer morphology by micro-computed X-ray tomography, Powder Technol., 273 (2015) 165-175 https://doi.org/110.1016/j.powtec.2014.1012.1050.
[30] L.A. Giannuzzi, D. Phifer, N.J. Giannuzzi, M.J. Capuano, Two-dimensional and 3-dimensional analysis of bone/dental implant interfaces with the use of focused ion beam and electron microscopy, J. Oral Maxillofac. Surg., 65 (2007) 737-747 https://doi.org/710.1016/j.joms.2006.1010.1025.

[31] Z. Rong, W. Sun, H. Xiao, G. Jiang, Effects of nano-SiO_2 particles on the mechanical and microstructural properties of ultra-high performance cementitious composites, Cement. Concrete. Comp., 56 (2015) 25-31 https://doi.org/10.1016/j.cemconcomp.2014.1011.1001.
[32] N. Bossa, P. Chaurand, J. Vicente, D. Borschneck, C. Levard, O. Aguerre-Chariol, J. Rose, Micro-and nano-X-ray computed-tomography: A step forward in the characterization of the pore network of a leached cement paste, Cement. Concrete. Res., 67 (2015) 138-147 https://doi.org/110.1016/j.cemconres.2014.1008.1007.
[33] A. Sheidaei, M. Baniassadi, M. Banu, P. Askeland, M. Pahlavanpour, N. Kuuttila, F. Pourboghrat, L. Drzal, H. Garmestani, 3-D microstructure reconstruction of polymer nano-composite using FIB–SEM and statistical correlation function, Compos. Sci.and Technol., 80 (2013) 47-54 https://doi.org/10.1016/j.compscitech.2013.1003.1001.
[34] R. Wirth, Focused Ion Beam (FIB) combined with SEM and TEM: Advanced analytical tools for studies of chemical composition, microstructure and crystal structure in geomaterials on a nanometre scale, Chem. Geol., 261 (2009) 217-229 https://doi.org/210.1016/j.chemgeo.2008.1005.1019.
[35] A.J. Kubis, G.J. Shiflet, R. Hull, D.N. Dunn, Focused ion-beam tomography, Metall. Mater. Trans. A, 35 (2004) 1935-1943 https://doi.org/1910.1007/s11661-11004-10142-11664.
[36] M. Nehler, F. Stoeckhert, A. Oelker, J. Renner, E. Saenger, Evaluating porosity estimates for sandstones based on X-ray micro-tomographic images, 1-48 https://doi.org/10.5194/se-2019-5148.
[37] J. Orloff, Focused Ion Beam Characterization Techniques, in: K.H.J. Buschow, R.W. Cahn, M.C. Flemings, B. Ilschner, E.J. Kramer, S. Mahajan, P. Veyssière (Eds.) Encyclopedia of Materials: Science and Technology, Elsevier, Oxford, 2001, pp. 3226-3231.
[38] N. Yao, Focused ion beam systems: basics and applications, Cambridge University Press, 2007 https://doi.org/10.1017/CBO9780511600302.
[39] C. Holzapfel, W. Schäf, M. Marx, H. Vehoff, F. Mücklich, Interaction of cracks with precipitates and grain boundaries: Understanding crack growth mechanisms through focused ion beam tomography, Scr. Mater., 56 (2007) 697-700 https://doi.org/610.1016/j.scriptamat.2006.1012.1025.
[40] (Dragonfly (2018). Dragonfly 3.6.1: A software platform for the intuitive inspection of multi-scale multi-modality image data. Object Research Systems (ORS) Incorporated, Montreal, Quebec, Canada http://www.theobjects.com/dragonfly/index.html.
[41] A. Śmieszek, A. Donesz-Sikorska, J. Grzesiak, J. Krzak, K. Marycz, Biological effects of sol–gel derived ZrO_2 and SiO_2/ZrO_2 coatings on stainless steel surface—In vitro model using mesenchymal stem cells, J. Biomater. Appl., 29 (2014) 699-714 https://doi.org/610.1177/0885328214545095.
[42] G. Wang, F. Meng, C. Ding, P.K. Chu, X. Liu, Microstructure, bioactivity and osteoblast behavior of monoclinic zirconia coating with nanostructured surface, Acta Biomater., 6 (2010) 990-1000 https://doi.org/1010.1016/j.actbio.2009.1009.1021.
[43] A. Pettersson, G. Marino, A. Pursiheimo, J.B. Rosenholm, Electrosteric stabilization of Al_2O_3, ZrO_2, and 3Y–ZrO_2 suspensions: effect of dissociation and type of polyelectrolyte, J. Colloid. Interface. Sci., 228 (2000) 73-81 https://doi.org/10.1006/jcis.2000.6939.
[44] M. Morks, Fabrication and characterization of plasma-sprayed HA/SiO_2 coatings for biomedical application, J. Mech. Behav. Biomed., 1 (2008) 105-111 https://doi.org/110.1016/j.jmbbm.2007.1004.1003
[45] R. Telle, F. Greffrath, R. Prieler, Direct observation of the liquid miscibility gap in the zirconia–silica system, J. Eur. Ceram. Soc., 35 (2015) 3995-4004 https://doi.org/3910.1016/j.jeurceramsoc.2015.3907.3015.
[46] F. Monte, W. Larsen, J.D. Mackenzie, Stabilization of tetragonal ZrO_2 in ZrO_2–SiO_2 binary oxides, J. Am. Ceram. Soc., 83 (2000) 628-634 https://doi.org/610.1111/j.1151-2916.2000.tb01243.x.
[47] P. Tartaj, C.J. Serna, J.S. Moya, J. Requena, M. Ocaña, S. De Aza, F. Guitian, The formation of zircon from amorphous ZrO_2-SiO_2 powders, J. Mater. Sci., 31 (1996) 6089-6094 https://doi.org/6010.1007/BF01152164.
[48] S. Zhang, N. Ali, Nanocomposite thin films and coatings: processing, properties and performance, Imperial college press, 2007 https://doi.org/10.1142/p502.
[49] J.B. Miller, S.E. Rankin, E. Ko, Strategies in controlling the homogeneity of zirconia-silica aerogels: effect of preparation on textural and catalytic properties, J. Catal., 148 (1994) 673-682 https://doi.org/610.1006/jcat.1994.1254.
[50] M. Mehdipour, A. Afshar, M. Mohebali, Electrophoretic deposition of bioactive glass coating on 316L stainless steel and electrochemical behavior study, Appl. Surf. Sci., 258 (2012) 9832-9839 https://doi.org/9810.1016/j.apsusc.2012.9806.9038.
[51] M. Farrokhi-Rad, Effect of morphology on the electrophoretic deposition of hydroxyapatite nanoparticles, J. Alloys Compd., 741 (2018) 211-222 https://doi.org/210.1016/j.apsusc.2012.1006.1038.
[52] H. Farnoush, J.A. Mohandesi, D.H. Fatmehsari, Effect of particle size on the electrophoretic deposition of hydroxyapatite coatings: a kinetic study based on a statistical analysis, Int. J. Appl. Ceram., 10 (2013) 87-96 https://doi.org/10.1111/j.1744-7402.2012.02818.x.

[53] P. Amrollahi, J.S. Krasinski, R. Vaidyanathan, L. Tayebi, D. Vashaee, Electrophoretic Deposition (EPD): Fundamentals and Applications from Nano- to Microscale Structures, in: M. Aliofkhazraei, A.S.H. Makhlouf (Eds.), Springer International Publishing, Cham, 2016, pp. 561-591 https://doi.org/510.1007/1978-1003-1319-15266-15260_15267.
[54] N. Sato, M. Kawachi, K. Noto, N. Yoshimoto, M. Yoshizawa, Effect of particle size reduction on crack formation in electrophoretically deposited YBCO films, Phys. C Supercond., 357–360, Part 2 (2001) 1019-1022 https://doi.org/1010.1016/S0921-4534(1001)00510-X.
[55] L. Besra, M. Liu, A review on fundamentals and applications of electrophoretic deposition (EPD), Prog. Mater. Sci., 52 (2007) 1-61 https://doi.org/10.1016/j.pmatsci.2006.1007.1001.
[56] A. Venugopal, J. Srinath, L.R. Krishna, P.R. Narayanan, S. Sharma, P. Venkitakrishnan, Corrosion and nanomechanical behaviors of plasma electrolytic oxidation coated AA7020-T6 aluminum alloy, Mater. Sci. Eng. A, 660 (2016) 39-46https://doi.org/10.1016/j.msea.2016.1002.1045.
[57] X. Lu, C. Blawert, K.U. Kainer, M.L. Zheludkevich, Investigation of the formation mechanisms of plasma electrolytic oxidation coatings on Mg alloy AM50 using particles, Electrochim. Acta, 196 (2016) 680-691 https://doi.org/610.1016/j.electacta.2016.1003.1042.
[58] J.W. Choi, G.W. Kim, K.R. Shin, B. Yoo, D.H. Shin, Synthesis of Zirconium–Titanium oxide mixed layers on Ti substrates by plasma electrolytic oxidation and plasma-enhanced electrophoresis, J. Alloys Compd., 726 (2017) 930-938 https://doi.org/910.1016/j.jallcom.2017.1008.1004.
[59] F. Walsh, C. Low, R. Wood, K. Stevens, J. Archer, A. Poeton, A. Ryder, Plasma electrolytic oxidation (PEO) for production of anodised coatings on lightweight metal (Al, Mg, Ti) alloys, Trans. Inst. Met. Finish., 87 (2009) 122-135 https://doi.org/110.1179/174591908X174372482.
[60] R. Phelan, J.D. Holmes, N. Petkov, Application of serial sectioning FIB/SEM tomography in the comprehensive analysis of arrays of metal nanotubes, J. Microsc., 246 (2012) 33-42 https://doi.org/10.1111/j.1365-2818.2011.03582.x.
[61] S. Fatimah, M. Kamil, J. Kwon, M. Kaseem, Y. Ko, Dual incorporation of SiO_2 and ZrO_2 nanoparticles into the oxide layer on 6061 Al alloy via plasma electrolytic oxidation: Coating structure and corrosion properties, J. Alloys Compd., 707 (2017) 358-364 https://doi.org/310.1016/j.jallcom.2016.1011.1098.
[62] T.C. Schumacher, L. Treccani, K. Rezwan, Effect of silica on porosity, strength, and toughness of pressureless sintered calcium phosphate–zirconia bioceramics, Biomed. Mater., 10 (2015) 045020 https://doi.org/045010.041088/041748-046041/045010/045024/045020.
[63] S. Lim, H.-S. Lee, S. Kawashima, Pore structure refinement of cement paste incorporating nanosilica: Study with dual beam scanning electron microscopy/focused ion beam (SEM/FIB), Mater. Charact., 145 (2018) 323-328 https://doi.org/310.1016/j.matchar.2018.1008.1045.
[64] B.J. McEntire, B.S. Bal, M.N. Rahaman, J. Chevalier, G. Pezzotti, Ceramics and ceramic coatings in orthopaedics, J. Eur. Ceram. Soc., 35 (2015) 4327-4369 https://doi.org/4310.1016/j.jeurceramsoc.2015.4307.4034.
[65] J. Barralet, L. Grover, T. Gaunt, A. Wright, I.R. Gibson, Preparation of macroporous calcium phosphate cement tissue engineering scaffold, Biomaterials, 23 (2002) 3063-3072 https://doi.org/3010.1016/S0142-9612(3001)00401-X.
[66] A. Kar, K.S. Raja, M. Misra, Electrodeposition of hydroxyapatite onto nanotubular TiO_2 for implant applications, Surf. Coat. Technol., 201 (2006) 3723-3731 https://doi.org/3710.1016/j.surfcoat.2006.3709.3008.
[67] S.-H. Oh, R.R. Finõnes, C. Daraio, L.-H. Chen, S. Jin, Growth of nano-scale hydroxyapatite using chemically treated titanium oxide nanotubes, Biomaterials, 26 (2005) 4938-4943 https://doi.org/4910.1016/j.biomaterials.2005.4901.4048
[68] V. Karageorgiou, D. Kaplan, Porosity of 3D biomaterial scaffolds and osteogenesis, Biomaterials, 26 (2005) 5474-5491 https://doi.org/5410.1016/j.biomaterials.2005.5402.5002.
[69] P.-I. Branemark, Osseointegration and its experimental background, J. Prosthet. Dent., 50 (1983) 399-410 https://doi.org/310.1016/S0022-3913(1083)80101-80102.
[70] A. Srinivasan, N. Rajendran, Electrochemical Corrosion and In Vitro Bioactivity of SiO_2: ZrO_2-Coated 316L Stainless Steel in Simulated Body Fluid, J. Mater. Eng. Perform., 24 (2015) 3056-3067 https://doi.org/3010.1007/s11665-11015-11587-x.
[71] M. Farhadian, K. Raeissi, M.A. Golozar, S. Labbaf, T. Hajilou, A. Barnoush, Electrophoretic deposition and corrosion performance of Zirconia-Silica composite coating applied on surface treated 316L stainless steel: Toward improvement of interface structure, Surf. Coat. Technol., 380 (2019) 125015 https://doi.org/125010.121016/j.surfcoat.122019.125015.
[72] N. Karimi, M. Kharaziha, K. Raeissi, Electrophoretic deposition of chitosan reinforced graphene oxide-hydroxyapatite on the anodized titanium to improve biological and electrochemical characteristics, Mater. Sci. Eng. C, 98 (2019) 140-152 https://doi.org/110.1016/j.msec.2018.1012.1136.